

# Estimating Joint Contact Areas and Ligament Lengths From Bone Kinematics and Surfaces

G. Elisabeta Marai\*, David H. Laidlaw, Çağatay Demiralp, Stuart Andrews, Cindy M. Grimm, and Joseph J. Crisco

**Abstract**—We present a novel method for modeling contact areas and ligament lengths in articulations. Our approach uses volume images generated by computed tomography and allows the *in vivo* and noninvasive study of articulations. In our method, bones are modeled both implicitly (scalar distance fields) and parametrically (manifold surfaces). Using this double representation, we compute interbone distances and estimate joint contact areas. Using the same types of representation, we model ligament paths; in our model, the ligaments are approximated by the shortest paths in a three-dimensional space with bone obstacles. We demonstrate the method by applying our contact area and ligament model to the distal radioulnar joints of a volunteer diagnosed with malunited distal radius fracture in one forearm. Our approach highlights focal changes in the articulation at the distal radioulnar joint (location and area of bone contact) and potential soft-tissue constraints (increased “length” of the distal ligaments and ligament-bone impingement in the injured forearm). Results suggest that the method could be useful in the study of normal and injured anatomy and kinematics of complex joints.

**Index Terms**—Computed tomography, contact areas, differential geometry, distance fields, joints, ligament paths.

## I. INTRODUCTION

WE PROPOSE a method for modeling bony contact areas and ligament paths in articulations. Contact areas define the cortical surface where bones articulate with each other. Modifications in bony contact areas and ligaments correlate with numerous joint-related post-trauma disabilities and various degenerative diseases, yet little information about the nature of these modifications is currently available. Most articulation and soft tissue studies are performed either *in vitro* or during clinical interventions and, thus, reveal little information on potential modifications of soft tissue biomechanics due to injury or disease. *In vitro* specimens illustrating a specific trauma or disease are rarely available; invasive studies inevitably alter joint kinematics and, thus, introduce false modifications. Although *in vivo* three-dimensional (3-D) techniques for studying the structure and kinematics of joint were recently introduced [1]–[4],

they do not attempt to capture more subtle details such as potential soft-tissue constraints or modifications in articulation. Our method successfully identifies and highlights *in vivo* and noninvasively potential focal changes and soft-tissue constraints in articulations.

In our approach, the structure and kinematics of an articulation are determined from segmented computed tomography (CT) volume images. Bones in the joint are modeled further both implicitly, as *scalar distance fields*, and parametrically, as *manifold surfaces*. These two types of representation have complementary strengths for different types of calculations. Manifold surfaces provide an accurate, smooth, and locally controllable representation of the bones [5]. Distance fields, on the other hand, have important advantages for geometric computations such as fast distance calculation, collision detection, and inside–outside tests [7]. Distance fields computed from the parametric representation provide the support for estimating contact areas. Once contact areas are calculated, focal changes in the articulation are evaluated by comparing the area and location of the bony contact.

We assess potential soft-tissue constraints by calculating the minimum “length” of ligaments as a function of bone kinematics. Ligament paths are also modeled based on the distance field representation. We model ligaments as shortest paths between ligament insertion points—the points at which a ligament is anchored to bones; these paths are constrained to avoid bone penetration. Our model takes into account the ligament fiber orientation, the location of the ligament insertion points, and the locations of adjacent bones. The ligament model reported here is based solely on joint geometry.

We demonstrate our method by applying it to data collected from both forearms of a volunteer diagnosed with a malunited distal radius fracture in one forearm. The distal radioulnar joint (DRUJ), a complex joint involved in forearm rotation, comprises the two forearm bones (radius and ulna; see Fig. 1) and a number of ligament and cartilaginous complexes. Forearm injuries involving the DRUJ often result in a significantly decreased range of rotational motion, decreased grip strength, and loss of wrist motion. The symptoms can be disabling, especially in physically active individuals or when the pathology affects a work-related activity.

Altered soft tissues and focal changes in the DRUJ articulation may be responsible for the abnormal functioning of the forearm in the absence of evident bone damage, as a recent study suggests [8]. We show that our contact-area and ligament-length model gives unexpected insight into the biomechanics of the forearm and, more importantly, reveals significant differences between uninjured and injured articulations at the DRUJ. Re-

Manuscript received August 19, 2002; revised September 1, 2003. This work was supported in part by the National Science Foundation under Grant CCR0093238 and by the National Institutes of Health under Grant AR44005. Asterisk indicates corresponding author.

\*G. E. Marai is with the Department of Computer Science, Brown University, Providence, RI 02912 USA (e-mail: gem@cs.brown.edu).

D. H. Laidlaw, Ç. Demiralp, and S. Andrews are with the Department of Computer Science, Brown University, Providence, RI 02912 USA.

C. M. Grimm is with the Department of Computer Science, Washington University, St. Louis, MO 63130 USA.

J. J. Crisco is with the Department of Orthopaedics and the Division of Engineering, Brown Medical School/Rhode Island Hospital, Providence, RI 02912 USA.

Digital Object Identifier 10.1109/TBME.2004.826606

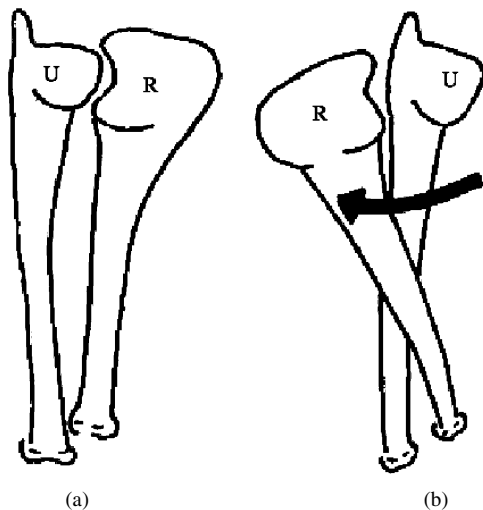


Fig. 1. DRUJ comprises the two forearm bones, radius (R) and ulna (U). Wrist is at the upper extremity of the drawing. During forearm rotation the DRUJ goes from (a) supination to (b) pronation.

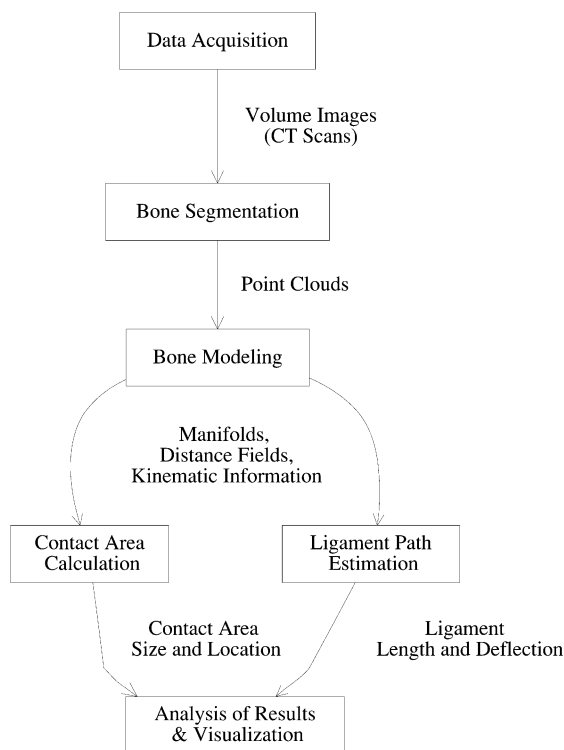


Fig. 2. Method pipeline for measurement of contact areas and ligament paths in joints. Point clouds corresponding to bone surfaces are segmented from CT volume images. Bones are further modeled as both distance fields and manifold surfaces. From the ligament-path and contact-area models, we extract information characterizing the articulation that is further analyzed and presented to the user.

sults indicate that our method could be useful in the study of the normal anatomy and kinematics of complex joints like the wrist and may also have applications to the study of other joints like the knee or the elbow.

## II. MATERIALS AND METHODS

Fig. 2 depicts our method pipeline. In the first phase, image volumes of the wrists in multiple poses are acquired with a CT

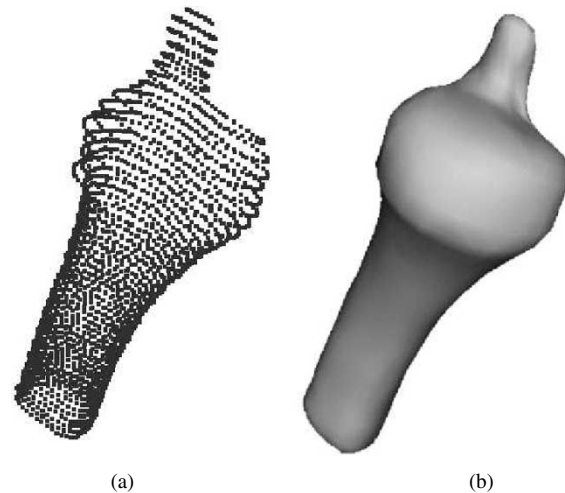


Fig. 3. Manifold surface representation of bones: (a) segmented point cloud corresponding to the ulna and (b) parametric (manifold) model of the same bone.

scanner (Section II-A). From these images, bones are manually segmented and further modeled as distance fields and manifold surfaces (Section II-B). Kinematic information is recovered via surface registration of the bones (Section II-C). Bony contact areas and ligament paths are estimated using both bone representations (Sections II-D and II-E). We repeat the contact-area and minimum-path computation over all joint poses for a given volunteer. Finally, contact areas and ligaments of the injured and uninjured forearm of the volunteer are compared (Section II-F).

### A. Data Acquisition

CT volume images of both wrists were obtained simultaneously with a GE HiSpeed Advantage CT scanner. Scout and reference scans were performed with the forearm and wrist in the neutral position. Additional scans were performed with the forearm at  $30^\circ$ ,  $60^\circ$ , and  $90^\circ$  of both pronation (i.e., forearm with the palm facing downwards) and supination (i.e., forearm with the palm facing upwards). In the forearm with limited mobility (decreased range of pronosupination), scans were made at  $30^\circ$  intervals and then at the maximum rotation that could be comfortably achieved. Approximately 45 1.0-mm CT slices were acquired at each position.

### B. Bone Segmentation and Modeling

Points corresponding to the outer bone cortex were manually segmented from each CT slice and grouped to form a separate 3-D point cloud for each bone. We reconstruct a bone surface by fitting a manifold surface to the corresponding cloud of 3-D points [5], (Fig. 3); the result is a smooth locally parameterized  $C^2$  continuous surface. The overlapped structure of the manifold-surface representation, which is essentially inspired by differential geometry, has several advantages including flexibility in shape adjustments without costly constraints and smooth transitions and uniformity among patches.

The manifold model addresses difficulties introduced by the CT scanning process, such as dense sampling along sparse contours and noise [5]. The manifold model is analytic and, therefore, can be sampled at any resolution to produce smooth distance maps. High-resolution smooth distance maps are

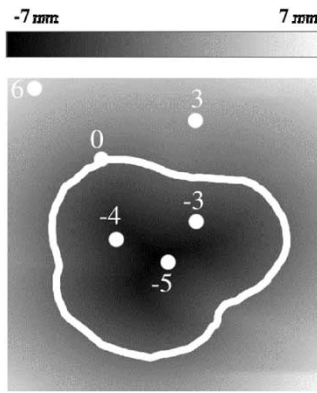


Fig. 4. Distance field representation of bones: horizontal 2-D section through a signed distance field (ulna). Contour corresponds to the boundary of the bone. Sign distinguishes the inside from the outside of the bone; negative values are inside the bone, positive values are outside the bone, zero values are on the bone surface. Dark area is the inside of the bone.

necessary in order to build ligament paths, as discussed in Section II-E.

By convention, we reflect left forearm data in order to directly compare it with right forearm data. The mirroring operation is purely mathematical and does not affect the data; it merely allows easier comparisons.

Modeling contact areas and ligament paths requires bone-to-bone distance information (Sections II-D and II-E). The manifold surfaces provide accurate, smooth, but computationally expensive distance information. We combine the manifold representation with interpolated distance fields, which are slightly less accurate but more intuitive and much faster.

Distance fields for each bone are computed using the reconstructed manifold bone models. A distance field is a scalar field that specifies the signed distance from a point to the bone surface (Fig. 4). A numerical sign is used to distinguish the inside from the outside of the bone; negative values are inside the bone, positive values are outside the bone, zero values are on the bone surface.

The distance field is computed from the manifold representation as follows: given a point  $P$  in space, the closest point  $Q$  on the manifold has the property that the surface normal at  $Q$  points in the direction  $P$ - $Q$ . We find an approximate guess for the point  $Q$  by finding the closest point  $Q$  on the manifold mesh, then perform a gradient descent to find the  $Q$  that meets the above criteria. The inside-outside test simply involves counting the number of intersections with the manifold mesh of any ray from  $P$  [6].

In order to increase the speed of lookup operations, the distance fields are sampled on a regular grid. We call the result a *distance cuboid*. The distance cuboid can be regarded as a scalar data set sampled over a regular 3-D grid surrounding the bone. Distances to the bone surface are known exactly at grid nodes. Within a grid cell, distances to the bone surface are obtained via tricubic B-spline interpolation of the distance values at grid nodes.

The double bone representation—manifold surfaces and distance cuboids—enables us to perform further joint-related computations, such as calculation of bony contact areas (Section II-D) and estimation of ligament paths (Section II-E).

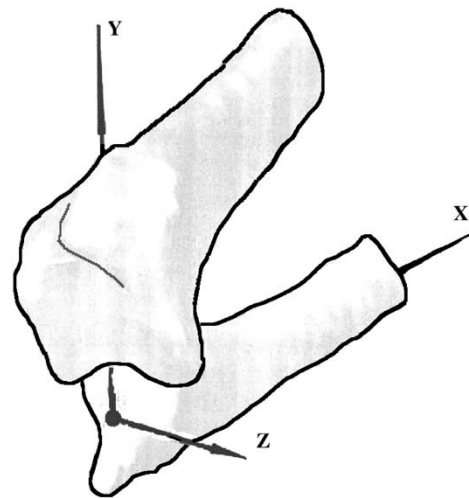


Fig. 5. Anatomic coordinate system defined on the ulna. Location and orientation of the  $x$  axis were generated from the diaphysal cross-section centroids of the ulna, while the  $z$  axis was defined to be perpendicular to a plane that passed through the  $x$  axis and the tip of the ulnar styloid.  $y$  axis was constructed perpendicular to both the  $x$  and  $z$  axes.

### C. Recovery of Bone Kinematics

Recovering the bone kinematics enables us to analyze our contact area and ligament measurements as functions of wrist motion. Motion of the radius with respect to the ulna was determined for each scanned wrist rotation position. First, the ulna bone was registered with respect to its neutral position to account for global changes in forearm positioning. Next, the relative motion of the radius with respect to the ulna was calculated. Registration is accomplished via a surface-distance-minimization algorithm [8]. Bone kinematics were reported in a standard anatomic coordinate system defined in the distal ulna as follows: the  $x$  axis was directed proximally along the shaft of the ulna and defined by the centroids of the ulnar bone cross sections, the  $z$  axis was in a palmar direction and defined to be perpendicular to a plane that passed through the  $x$  axis and the tip of the ulnar styloid, and the  $y$  axis was constructed perpendicular to both the  $x$  and  $z$  axes. The origin of the coordinate system was defined by the intersection of the  $x$  axis with the (ulnocarpal) articular surface of the head of the ulna (Fig. 5).

### D. Contact Area Calculation

The bony contact area is defined as the cortical surface area on the bone that is less than a prescribed threshold distance (typically 5 mm) from the cortical surface of a neighboring bone. Estimating contact areas requires computation of interbone distances within the joint.

Once distance cuboids are generated, we calculate the distance from an arbitrary point  $p$  and a bone surface  $b$  as follows. Each bone surface has a surrounding distance cuboid  $f_b$ . We remind the reader that a distance cuboid can be regarded as a sampled dataset stored over a regular 3-D grid; distance values are known exactly at grid nodes and computed via interpolation inside grid cells.

The point  $p$  can be inside or outside the distance cuboid  $f_b$ . We make sure that areas of interest (i.e., articulated surfaces) are well within the distance cuboid. For simplicity, Fig. 6 illustrates

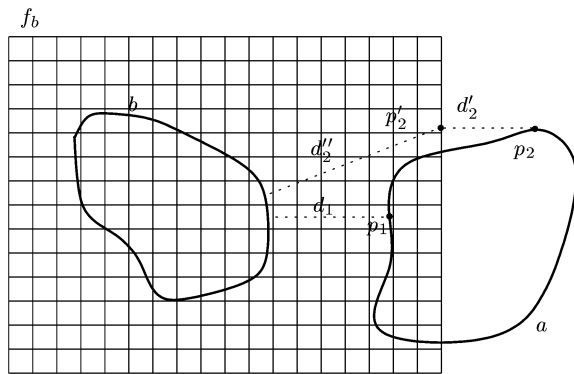


Fig. 6. Two-dimensional illustration for obtaining distances from points  $p_1$  and  $p_2$  to bone  $b$ .  $f_b$  is the distance cuboid for bone  $b$ . Shortest distance values to bone  $b$  at the grid intersections are known. We use tricubic interpolation to determine distance values within the grid. Since  $p_1$  is inside the cuboid, the distance from  $p_1$  to  $b$  is equal to  $f_b(p_1) = d_1$ . For  $p_2$ , we first find the distance to the closest point  $p_2'$  in the distance cuboid, and then the distance between  $p_2$  and  $b$  is approximated as  $d_2'' + f_b(p_2') = d_2'' + d_2'$ .

the procedure in two dimensions. We evaluate two cases to find the distance.

**$p$  is inside  $f_b$ :** we look up  $f_b$  for  $p$ .

**$p$  is outside  $f_b$ :** we first find the distance to the nearest point  $p'$  on the boundary of  $f_b$ . We then add it to the distance value acquired by looking up  $f_b$  for  $p'$ . Since points outside the distance cuboid are of little interest (i.e., they are far away from articulated surfaces), this distance sum is an acceptable approximation.

With this procedure, we find distances from every vertex in the surface model of one bone to neighbors of interest.

Using the interbone distance, we compute isocontours on the contact area, each contour showing where the distance map is equal to a constant distance. For efficient computation, we assume that the distance map is linear over the triangular faces that comprise the surface of the bone and, thus, the equal distance contours are straight-line segments over each triangle. If the distance value of a contour is within the range of the distance values at the vertices, a contour line segment is generated over the triangle.

Fig. 7 shows typical contact areas in the DRUJ; the joint was exploded to show the articulated surfaces more clearly. The color on bone surfaces codifies the distance to the nearest point on the opposite bone; darker regions are closer.

We characterize the contact area by its size and by the location of its centroid. The size is the area of the surface triangles within the 5-mm contour. The location of the centroid is described in cylindrical coordinates with respect to the same standard coordinate system used to report bone kinematics.

It is important to note that the articular contact calculated here is an estimate of joint contact based upon the distance between cortical bone surfaces. Cartilage thickness, bone and cartilage deformation, and stresses in the tissues were not considered in this study.

### E. Ligament Path Estimation

We can also use the double-bone representation to construct ligament paths. We use anatomical landmarks to manually iden-

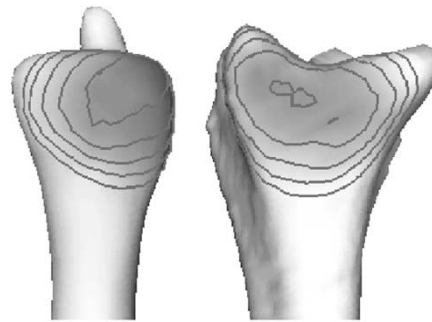


Fig. 7. Contact areas in the DRUJ. Bones are color mapped and contoured. Color saturation on bone surfaces indicates the distance to the nearest point on the opposite bone; darker regions are closer. Joint is exploded to show the articulated surfaces more clearly. Maximum distance visualized is 5 mm; contour lines are drawn at 1-mm intervals.

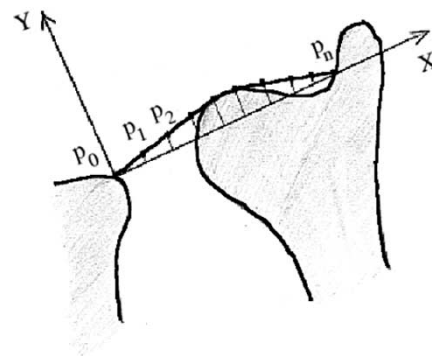


Fig. 8. Shortest path between two points  $p_0$  and  $p_n$  (2-D case); path must not penetrate the 2-D obstacle on the right. Following the optimization approach, the points  $p_1$  to  $p_{n-1}$ , initially equally distributed on the  $p_0p_n$  segment, increase their  $y$  coordinate so that the nonpenetration constraint is satisfied.

tify the insertion points (the points where the ligament is anchored to the bone) of a given ligament on the bone surface. We generate plausible ligament paths as shortest paths between insertion points, constrained to avoid bone penetration.

We build shortest paths via an optimization approach that exploits the distance-field representation of the bones. Unlike other possible minimum-path approaches, this technique deals effectively with a large number of bone model vertices without requiring expensive restructuring—in terms of memory and time—of the search space. The resulting paths are also more accurate than those generated, for example, by graph approximation algorithms, as the method allows a large number of path control points and recovers gracefully from obstacle penetration. We begin the description of the algorithm with a simplified 2-D example, shown in Fig. 8. Here, we are required to find a shortest path between two points  $p_0$  and  $p_n$  that does not penetrate the 2-D obstacle on the right.

We start by attaching a local 2-D coordinate system to the obstacle, so that the origin of the system is at  $p_0$  and the  $x$  axis is the line defined by  $p_0$  and  $p_n$ . We consider  $n-1$  points in addition to  $p_0$  and  $p_n$ , equally spaced on the  $p_0p_n$  segment. We reformulate our problem in the following terms: Find the coordinates of the  $n-1$  points so that the length of the path  $p_0p_1p_2 \dots p_n$  is minimum and the height of each point with respect to the obstacle surface is nonnegative. If we fix the  $x$  coordinates of the

points so that they are initially equally spaced on the  $p_0p_n$  segment, our problem amounts to minimizing the Euclidean length of the path over the  $y_i$  coordinates of the points

$$\begin{aligned} & \operatorname{argmin}_{y_i} \sum_{i=0}^{n-1} \sqrt{(x_{i+1} - x_i)^2 + (y_{i+1} - y_i)^2} \\ & = \operatorname{argmin}_{y_i} \sum_{i=0}^{n-1} \sqrt{\text{const} + (y_{i+1} - y_i)^2} \\ & \text{subject to } f_b(x_i, y_i) > 0, \quad i = 0 \dots n - 1 \end{aligned}$$

where  $x_{i+1} - x_i = \text{const}, i = 0 \dots n - 1$ .

The formulation described above extends to three dimensions, where we optimize over both the  $y$  and  $z$  coordinates of the points

$$\begin{aligned} & \operatorname{argmin}_{y_i, z_i} \sum_{i=0}^{n-1} \sqrt{\text{const} + (y_{i+1} - y_i)^2 + (z_{i+1} - z_i)^2} \\ & \text{subject to } f_b(x_i, y_i, z_i) > 0, \quad i = 0 : n - 1. \end{aligned}$$

The extension of the algorithm to any number of obstacles is straightforward.

We use a sequential quadratic programming method [9] to solve the optimization problem. The sequential quadratic programming method is fast and robust and handles both nonlinear objective functions and nonlinear constraints. Although it is a general concern that nonlinear optimizations can become trapped in suboptimal local solutions, in our experience this has not been a problem. We have found that additional iterations of the optimization process with significantly different start positions converge to the same solution. We are currently using three different start solutions:

- 1) points on the straight  $p_0p_n$  line;
- 2) points on a randomly displaced path;
- 3) points generated by the procedure in the previous pronosupination position.

The optimization procedure converges to the same solution in all three cases. This outcome is justified by the smooth structure and fine resolution of the search space generated by the distance-field representation.

We considered several plausible insertion points for each ligament, as precise information on insertion point location was not available. The insertion points were generated by randomly distributing points around a manually chosen landmark on the surface of the bones, within a circular area with a diameter of 4 mm (Fig. 9). The insertions were defined on the ulna at the base of the styloid for both ligaments and on the radius at the dorsal and palmar prominences of the sigmoid notch, respectively. The locations of the insertion sites and the area of insertion were derived from anatomical descriptions in the literature [33]–[36]. The results of the insertion-point study are presented in Section III.

We tried several values for the number of points  $n$ . In the DRUJ case, as  $n$  approaches 40 the total length of the path converges to a stable value. For this value of  $n$ , the length of each minisegment in the path drops below 0.2 mm, which provides sufficient accuracy to detect deflection of the ligament by the bone. Fig. 10 shows two shortest paths generated with our algorithm.

We characterize the ligament paths by their lengths and their “deflection.” Lengths are normalized with respect to the uninjured length in neutral pronosupination. Deflection is defined as

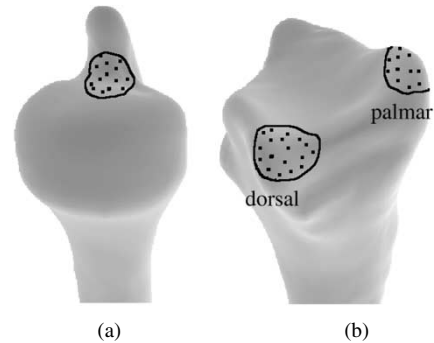


Fig. 9. Insertion point location. Insertion points are chosen manually, based on anatomical information. Points are randomly distributed on the surface of the bones within a circular area with a diameter of 4 mm. (a) Insertion site on the ulna. (b) Dorsal and palmar insertion sites on the radius.

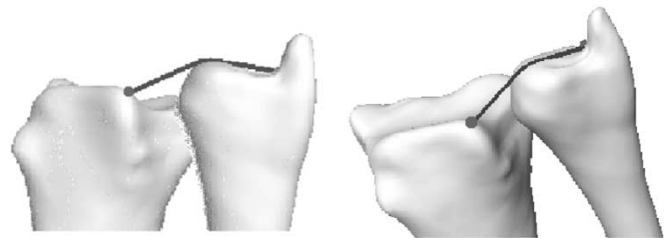


Fig. 10. Shortest paths (dark gray lines) generated by the ligament model.

the maximum distance across all path points to the straight line defined by the two ligament insertion points.

The ligament-length model reported here is based solely on joint geometry. Structural and material properties of the ligaments were not taken into account in this study. While the paths we generate are not actual ligament paths, they give a useful lower bound on the length of these ligaments and, thus, help identify potential joint mobility constraints imposed by ligaments.

#### F. Visualization and Analysis of Results

The software package we have developed for visualizing the results of our technique consists of C++ and Open Inventor code and runs on the SUN UltraSparc and Windows platforms.

We visualize contact areas using color mapping and contouring. Color maps are generated for each bone so that distance values of surface points are mapped to varying color saturations (more saturated colors represent shorter distances). Distances larger than the contact threshold value (5 mm) are neither colored nor contoured and are shown as white surfaces. Contours and ligament paths are visualized as polylines.

We also analyze the results quantitatively by comparing ligament length, ligament deflection, contact area size, and contact area centroid location between the injured—malunited distal radius fracture—and uninjured forearm of the same volunteer.

### III. RESULTS AND DISCUSSION

Generating contact areas over different forearm rotation positions yields sequences like those in Fig. 11. The decreased size and shifted location of the bony contact area in the injured case is noticeable, especially toward pronation.

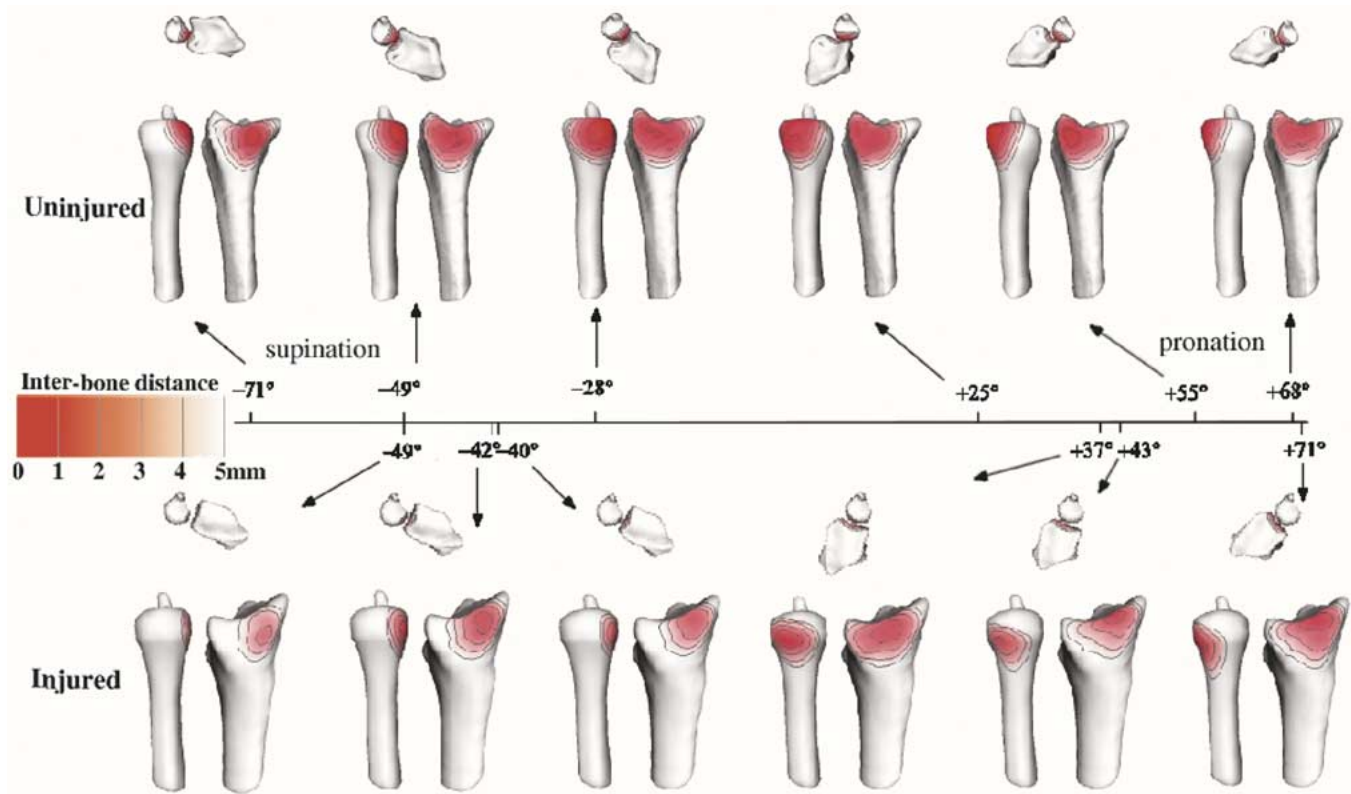


Fig. 11. Proximal and exploded lateral views of an uninjured and an injured radioulnar joint at six rotation positions. Bones are colored according to the distance between them (the closer they are, the more intense the color). Note the shift in the location of the contact areas between the uninjured and the injured forearm.

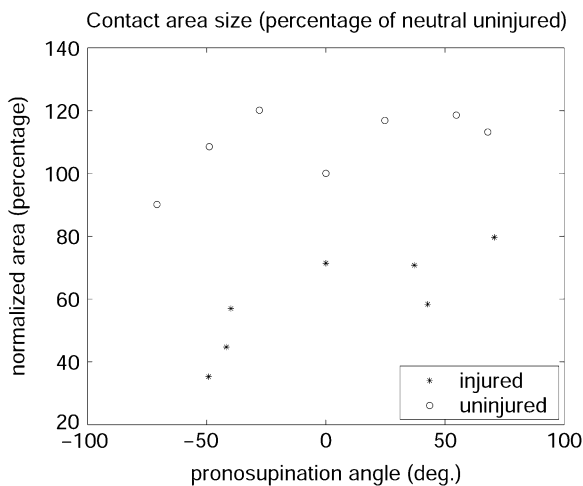


Fig. 12. Size of the ulnar contact area (5-mm threshold) for both the injured and uninjured forearm of the same volunteer. Areas are normalized by the neutral uninjured area. Pronosupination angles are shown on the *x* axis. Note the difference in size between the injured and uninjured forearm.

Fig. 12 quantifies the size of the ulnar contact area at a threshold of 5 mm for the volunteer’s uninjured and injured forearm. For the uninjured wrist, contact area was positive for a 3-mm threshold as well. For the injured wrist, there were several poses, mostly pronated, in which the 3-mm contact area was absent. Together with the 5-mm contact area changes, this suggests an increased gap between the bones in the injured case.

We measured contact area as a region on the ulnar surface close to the radius; an analogous measure on the surface of the radius can also be defined. We found that the area measure was somewhat larger (10%–20%), but followed the same trends as the ulnar contact area. The size difference is consistent with the concave contact area on the radius, which is larger because it is farther from the center of curvature than the corresponding area on the ulna. Measures based on the ulnar area are reported because they reside in the ulnar coordinate system; the ulnar coordinate system was chosen because it is stationary during pronosupination.

Fig. 13 shows the cylindrical coordinates of the ulnar contact area centroid for the uninjured and injured forearm. The increased height coordinate in the injured forearm confirms a shift of the contact area in the proximal direction. The increased distance from the ulnar axis is due to the shift of the contact area on the surface of the ulna to a region of the ulna further from the axis. The angle coordinate plot correlates with the limited range of motion in the injured forearm. The proximal shift in the location of the centroid of the contact area is consistent with the initial diagnosis of radial shortening.

Fig. 14 shows distal ligament paths generated for the injured and uninjured forearms of the same volunteer. The lengths generated by our approach are similar to those reported in *in vitro* studies; no *in vivo* information is currently available, to the best of our knowledge. Note that the injured forearm presents ligament-bone impingement for both the dorsal and the palmar ligament. No deflection of the ligaments by the bone is present in the uninjured forearm in any of the rotation positions. Fig. 15

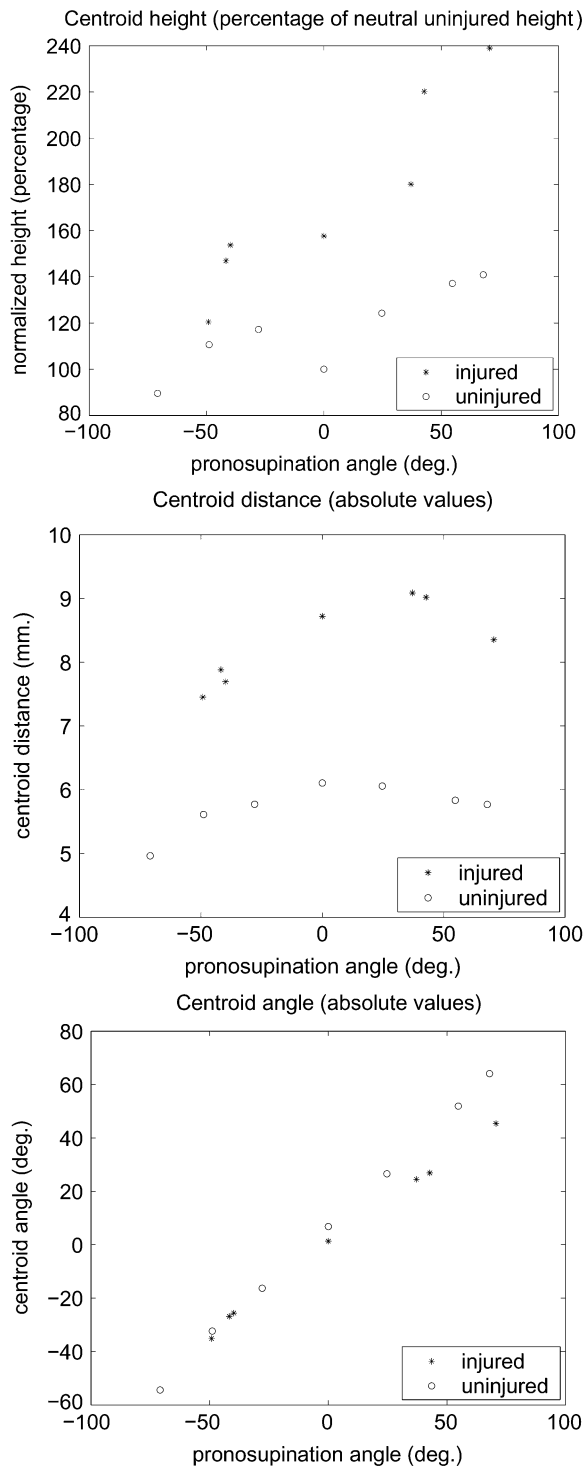


Fig. 13. Cylindrical coordinates (height, distance, and angle) of the ulnar contact area centroid for the injured and uninjured forearms of the volunteer. Heights are normalized by the neutral uninjured height. Pronosupination angles are shown on the  $x$  axis. Note the difference in height and distance between the injured forearm ligament and the uninjured forearm.

shows the dorsal radioulnar ligament length and deflection corresponding to the entire pronosupination sequence for the injured forearm. We also show the corresponding lengths and deflection computed for the matching uninjured forearm—note the difference between the two plots. Ligament impingement (measured by the deflection parameter) correlates with ligament

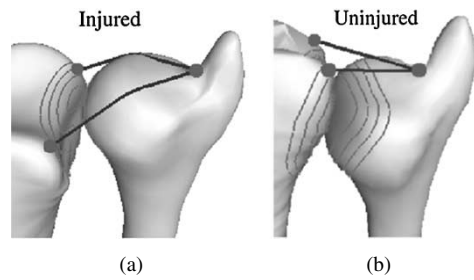


Fig. 14. Distal radioulnar ligament paths in (a) injured forearm and in (b) matching uninjured forearm of the same volunteer. Both forearms are in neutral pronosupination ( $0^\circ$  rotation angle). Note the ligament-bone impingement in the injured forearm; both ligaments are deflected by the head of the ulna.

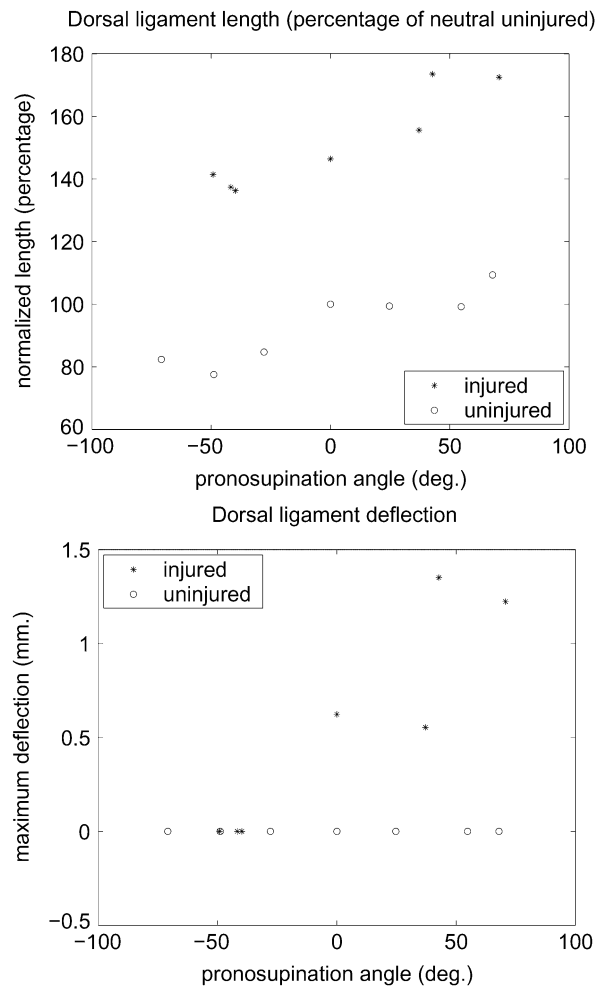


Fig. 15. (top) Length and (bottom) maximum deflection of a dorsal ligament for the injured and uninjured forearms of a volunteer. Lengths are normalized by the neutral uninjured length. Pronosupination angles are shown on the  $x$  axis. Note the increased ligament length in the injured forearm. Note also that no deflection is present in the uninjured forearm.

path increased length. No ligament deflection is present in the uninjured forearm. The dorsal ligament results generated by displacing the insertion points within the insertion site are plotted in Fig. 16. Note that perturbations in the ligament attachment locations do not affect trends in the comparison measures between the injured and uninjured forearms.

Fig. 17 shows plots of the palmar radioulnar ligament length and deflection. Although the palmar ligament length plot shows

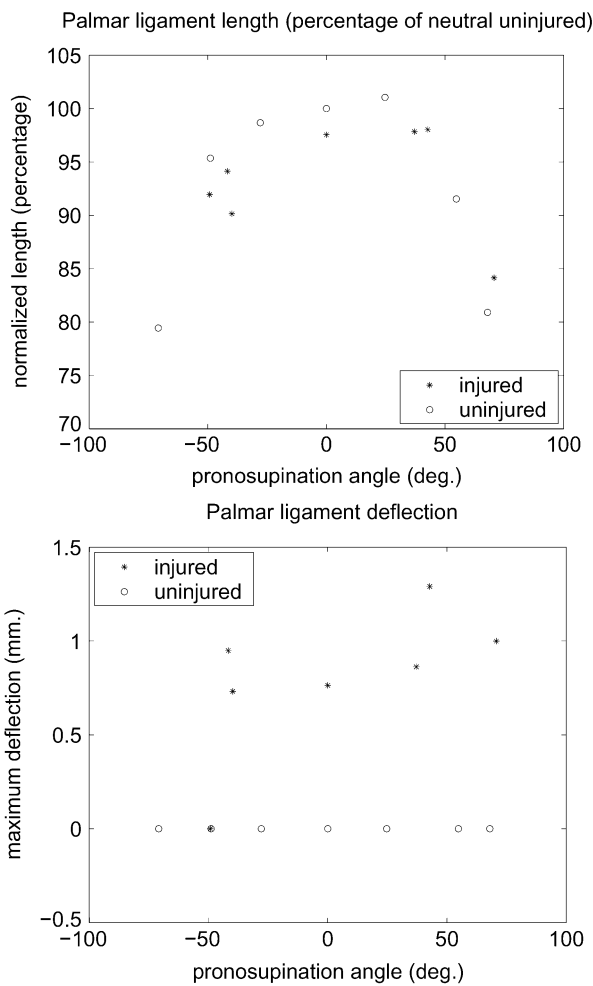


Fig. 16. Effect of insertion point perturbation on (top) the length and (bottom) the maximum deflection of a dorsal ligament for the injured and uninjured forearms of a volunteer (mean and standard deviation calculated over 64 measurements).

no difference between the injured and uninjured forearm, we note the impingement (deflection) in the injured forearm, lacking in the uninjured case. The palmar ligament results generated by perturbing the insertion points within the 4-mm diameter insertion sites are plotted in Fig. 18. Note again that perturbations in the ligament attachment locations do not affect trends in the comparison measures between the injured and uninjured forearms.

The change in the dorsal radioulnar ligament length, but not in the palmar radioulnar ligament length, is consistent with the original malunion (radius tilted dorsally). The change in ligament length and the ligament-bone impingement may be one mechanism for the limitation of forearm mobility.

While a single example cannot distinguish between normal anatomical variation and pathological variation, clinical studies on larger sets of patients may establish or refute a correlation between the differences we found here and the injury. Such studies are beyond the scope of this paper.

#### IV. RELATED WORK

Several approaches to modeling joint surfaces are known; thin-plate splines [19], B-splines [20], [21], and piecewise

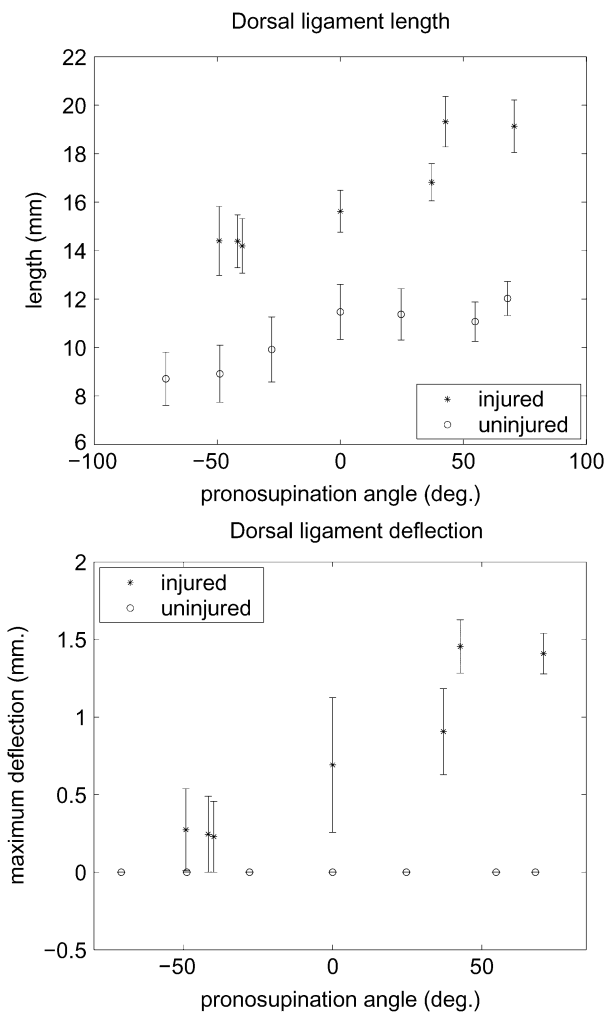


Fig. 17. (top) Length and (bottom) maximum deflection of a palmar ligament for the injured and uninjured forearms of a volunteer. Lengths are normalized by the neutral uninjured length. Pronosupination angles are shown on the  $x$  axis. Note that no deflection is present in the uninjured forearm.

patches [22] are among them. These methods suffer from problems such as lack of generality, lack of  $C^2$  continuity, and difficulty in enforcing boundary constraints. Our parametrical model for bone surfaces is based on manifolds [23].

Distance fields have been used in robotics [10], [11] and computer graphics [7], [12]–[15]. Although, for the results reported in this paper, we used a brute-force approach to generate distance cuboids from the manifold representation, faster techniques such as level set-based methods [16]–[18] are available.

Searching for shortest paths in spaces with obstacles is a classical problem in robotics. A survey of the substantial literature on the shortest-path problem can be found in [31]. Solutions are based on computational geometry methods [24]–[27], graph search-based algorithms [30], and differential geometry and hybrid techniques [28], [29], depending primarily on the assumed structure of the search space (polyhedral or continuous surfaces). Our technique belongs to the differential geometry and hybrid category. In general, methods in this class generate shortest paths on surfaces. These methods assume a continuous representation of surfaces and are, therefore, more accurate, al-



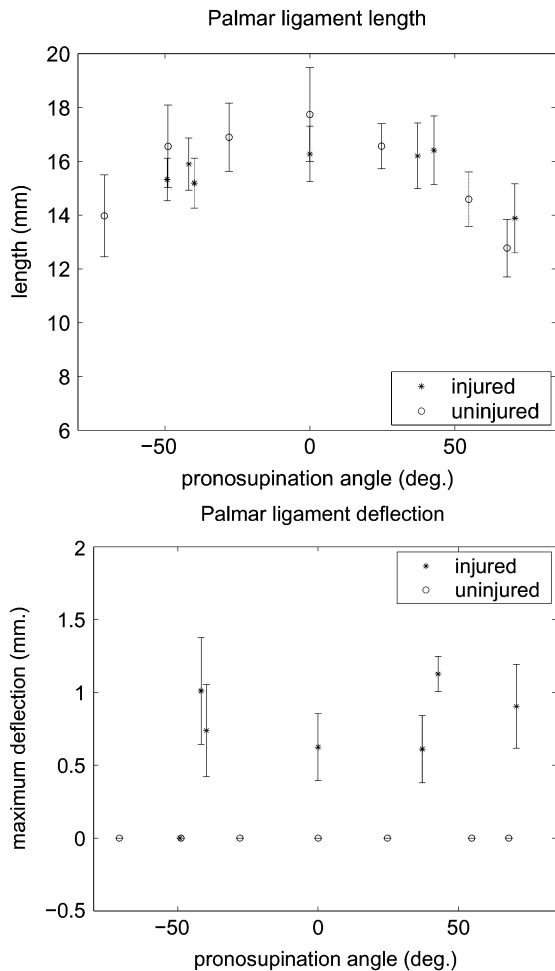


Fig. 18. Effect of insertion point perturbation on (top) the length and (bottom) the maximum deflection of a palmar ligament for both the injured and uninjured forearm of a volunteer (mean and standard deviation calculated over 64 measurements).

though they yield paths that are only locally optimal. Our work extends this approach to 3-D spaces with continuous surface obstacles.

The two scalar data visualization techniques we use, color mapping and isocontouring, are well-known scientific visualization techniques [32].

Studies of distal radioulnar ligaments are performed, in general, on cadaver uninjured wrists [33]–[35]. A clinical *in vivo* study involving surgery was performed by Kleinman *et al.* in 1998 [36]. To our knowledge, no *in vivo* noninvasive studies of the distal radioulnar ligaments have been done.

## V. CONCLUSION

We have demonstrated an *in vivo*, noninvasive technique for modeling the length of ligaments and joint contact areas from bone kinematics and surfaces. Our method uses an implicit model as well as a parametric surface model for each bone. The two types of representation have complementary strengths for different types of calculations. The double representation enables us to model secondary types of information from CT data, such as joint contact areas, intrajoint distances, and plausible ligament paths. Our current ligament model could be enriched

by considering other intrinsic and extrinsic ligament factors like tissue composition, muscle forces, and joint compression.

In a demonstration on the DRUJ, our approach highlights subtle modifications, otherwise unnoted, in injured wrist kinematics. Although a previous kinematic study [8] on the same data we analyze in this paper found no significant differences in rigid body kinematics between the injured and uninjured wrist, our method identified potential soft tissue constraints and focal changes in the articulation. The methods presented have the potential to document changes in the joint mechanics that may influence long-term clinical outcome.

Our technique may have applications to the study of wrist disorders such as rheumatoid arthritis, intercarpal ligament tear or attenuation, and carpal-tunnel syndrome. Results suggest that our technique could also be useful in the study of normal anatomy and kinematics of other joints.

## REFERENCES

- [1] C. P. Neu, R. D. McGovern, and J. J. Crisco, "Kinematic accuracy of three surface registration methods in a three-dimensional wrist bone study," *J. Biomech. Eng.*, vol. 122, pp. 1–6, 2000.
- [2] F. Eckstein, A. Gavazzeni, H. Sittek, M. Haubner, A. Losch, S. Milz, K. H. Englmeier, E. Schulte, R. Putz, and M. Reiser, "Determination of knee joint cartilage thickness using three-dimensional magnetic resonance chondro-crassometry (3d MR-CCM)," *Magn. Reson. Med.*, vol. 36, pp. 256–265, 1996.
- [3] V. Feipel, M. Rooze, S. Louryan, and M. Lemort, "Bi- and three-dimensional CT study of carpal bone motion in lateral deviation," *Surg. Radiol. Anat.*, vol. 14, pp. 381–389, 1992.
- [4] S. L. Van Sint Jan, G. J. Clapworthy, and M. Rooze, "Visualization of combined motions in human joints," *IEEE Comput. Graphics Applicat.*, pp. 10–14, Nov./Dec. 1998.
- [5] C. Grimm, J. J. Crisco, and D. H. Laidlaw, "Fitting locally parametric surfaces to 3D point clouds," *ASME J. Biomech. Eng.*, vol. 124, no. 1, pp. 136–40, 2002.
- [6] P. Alexandroff, *Elementary Concepts of Topology*. New York: Dover, 1961.
- [7] S. F. Frisken, R. N. Perry, A. P. Rockwood, and T. R. Jones, "Adaptively sampled distance fields: A general representation of shape for computer graphics," in *SIGGRAPH 2000 Conf. Proc.*, 2000, pp. 249–254.
- [8] D. Moore, K. Hogan, J. Crisco, E. Akelman, M. DaSilva, and A. Weiss, "3-D *in vivo* kinematics of the distal radioulnar joint in malunited distal radius fractures," *J. Hand Surg.*, vol. 27, no. 2, pp. 233–242, 2002.
- [9] NAG Fortran Library Routine Document [Online]. Available: <http://www.nag.co.uk/numeric/fl/manual/html/e04ucf.html>
- [10] R. Kimmel, N. Kiryati, and A. Bruckstein, "Multivalued distance maps for motion planning on surfaces with moving obstacles," *IEEE Trans. Robot. Automat.*, vol. 14, pp. 427–436, June 1998.
- [11] J. Lengyel, M. Reichert, B. Donald, and D. Greenberg, "Real-time robot motion planning using rasterizing computer graphics hardware," in *Proc. SIGGRAPH 1990*, 1990, pp. 327–335.
- [12] S. Gibson, "Using distance maps for smooth surface representation in sampled volumes," in *Proc. 1998 IEEE Volume Visualization Symp.*, 1998, pp. 23–30.
- [13] D. Breen, S. Mauch, and R. Whitaker, "3D scan conversion of CSG models into distance volumes," in *Proc. 1998 IEEE Symp. Volume Visualization*, 1998, pp. 7–14.
- [14] B. Payne and A. Toga, "Distance field manipulation of surface models," *IEEE Comput. Graphics Applicat.*, pp. 65–71, Jan. 1992.
- [15] A. Guezic, "Meshsweeper: Dynamic point-to-polygonal-mesh distance and applications," *IEEE Trans. Visualization Comput. Graphics*, vol. 7, no. 1, pp. 47–61, Jan.-Mar. 2001.
- [16] S. Osher and J. Sethian, "Fronts propagating with curvature-dependent speed: Algorithms based on Hamilton-Jacobi formulation," *J. Computational Phys.*, vol. 79, pp. 12–49, 1988.
- [17] J. Sethian, *Level Set Methods: Evolving Interfaces in Geometry, Fluid Mechanics, Computer Vision, and Material Science*. Oxford, U.K.: Cambridge Univ. Press, 1996.
- [18] —, "A fast marching level set method for monotonically advancing fronts," *Proc. Nat. Acad. Sci.*, vol. 94, pp. 1591–1595, 1996.

- [19] S. K. Boyd, J. L. Ronsky, D. D. Lichti, D. Salkauskas, and M. A. Chapman, "Joint surface modeling with thin-plate splines," *J. Biomech. Eng.*, vol. 121, pp. 525–532, Oct. 1999.
- [20] G. A. Ateshian, "A b-spline least-squares surface fitting method for articular surfaces of diarthrodial joints," *ASME J. Biomech. Eng.*, vol. 115, pp. 366–373, 1993.
- [21] ———, "Generating trimmed b-spline models of articular cartilage layers from unordered 3D surface data points," in *Proc. ASME Bioeng. Conf.*, 1995, pp. 217–218.
- [22] P. K. Scherrer and B. M. Hillberry, "Piece-wise mathematical representations of articular surfaces," *J. Biomechan.*, vol. 12, pp. 301–311, 1979.
- [23] C. Grimm and J. Hughes, "Modeling surfaces of arbitrary topology using manifolds," *Comput. Graphics*, vol. 29, no. 2, July 1995.
- [24] M. Scharir and A. Schorr, "On shortest paths in polyhedral spaces," *SIAM J. Comput.*, vol. 1, no. 15, pp. 193–215, 1986.
- [25] C. H. Papadimitriou, "An algorithm for shortest-path motion in three dimensions," *Inform. Processing Lett.*, vol. 20, pp. 259–263, 1985.
- [26] K. Clarkson, "Approximation algorithms for shortest path motion planning," in *Proc. 19th Annual SIGACT Symp.*, 1987, pp. 56–65.
- [27] A. Baltan and M. Scharir, "On shortest paths between two convex polyhedra," in *JACM*, vol. 35, 1988, pp. 267–287.
- [28] R. Kimmel and N. Kiryati, "Finding shortest paths on surfaces by fast global approximation and precise local refinement," *Int. J. Pattern Recogn. Artificial Intell.*, vol. 10, no. 6, pp. 643–656, 1996.
- [29] J. M. Beck, R. T. Farouki, and J. K. Hinds, "Surface analysis methods," *IEEE Comput. Graphics Applicat.*, vol. CGA-6, pp. 18–37, 1986.
- [30] N. Kiryati and G. Szekely, "Estimating shortest paths and minimal distance on digitized three dimensional surfaces," *Pattern Recogn.*, vol. 26, pp. 1623–1637, 1993.
- [31] C. K. Yap, "Algorithmic motion planning," *Advance Robot.*, vol. I, 1985.
- [32] K. Martin, W. Schroeder, and B. Lorensen, *The Visualization Toolkit: An Object-Oriented Approach to 3D Graphics*. Englewood Cliffs, NJ: Prentice-Hall, 1997.
- [33] F. Ekenstam, "Anatomy of the distal radioulnar joint," *Clin. Orthop.*, vol. 275, pp. 14–18, 1992.
- [34] R. Acosta, W. Hnat, and L. R. Sheker, "Distal radio-ulnar ligament motion during supination and pronation," *J. Hand Surg. (Br. Eur. Vol.)*, vol. 18B, pp. 502–505, 1993.
- [35] F. Schuind, K. An, L. Berglund, R. Rey, W. Cooney, R. Linscheid, and E. Chao, "The distal radioulnar ligaments: A biomechanical study," *J. Hand Surg.*, vol. 16A, no. 6, pp. 1106–1114, 1991.
- [36] W. Kleinman and T. Graham, "The distal radioulnar joint capsule: Clinical anatomy and role in posttraumatic limitation of forearm rotation," *J. Hand Surg.*, vol. 23A, no. 4, pp. 588–599, 1998.



**G. Elisabeta Marai** received the B.S. degree in computer science from Politehnica University of Bucharest, Bucharest, Romania, in 1997 and the Sc.M. degree in computer science from Brown University, Providence, RI, in 2001. She is working toward the Ph.D. degree at Brown University.

Her research interests include computer graphics and scientific visualization, with a focus on visualization, modeling, and automated analysis of medical data.



**David H. Laidlaw** received the Ph.D. degree in computer science from the California Institute of Technology, Pasadena, where he also did postdoctoral work in the Division of Biology.

He is an Associate Professor in the Computer Science Department, Brown University, Providence, RI. His research interests include applications of visualization, modeling, computer graphics, and computer science to other scientific disciplines.



**Çağatay Demiralp** received the B.S. degree in computer science from Ege University, Turkey, in 2000. He is working toward the M.S. degree in computer science at Brown University, Providence, RI.

His research interests include medical image registration, computer graphics, scientific visualization, and evaluation of virtual reality display systems.



**Stuart Andrews** received the B.S. degree in computer science from Toronto University, Toronto, ON, Canada, in 1999 and the Sc.M. degree in computer science from Brown University, Providence, RI, in 2001. He is working toward the Ph.D. degree at Brown University.

His research interests include machine learning and image retrieval.



**Cindy M. Grimm** received the B.A. degree in art and computer science from the University of California, Berkeley, in 1990 and the Ph.D. degree from Brown University, Providence, RI, in 1995.

She is an Assistant Professor in the Computer Science and Engineering Department, Washington University, St. Louis, MO. Her research interests include surface modeling and art-based rendering. She also spent two years doing postdoctoral work at Microsoft Research in the area of facial modeling and animation.



**Joseph J. Crisco** received the B.A. degree in mathematics and fine art from Amherst College and the Ph.D. degree in engineering and applied science from Yale University, New Haven, CT.

He is the Director of the Bioengineering Laboratory, Department of Orthopaedics, Brown University/Rhode Island Hospital, Providence, RI. His research interests include the biomechanics of the musculoskeletal system and sports injury.